Intrasession Reliability of Arterial Spin-Labeled MRI–Measured Noncontrast Perfusion in Glioblastoma at 3 T

Limin Zhou[1], Yiming Wang[1], Marco C. Pinho[1,2], Edward Pan[3,4,5], Yin Xi[1,6], Joseph A. Maldjian[1,2], and Ananth J. Madhuranthakam[1,2]

[1]Department of Radiology; [2]Advanced Imaging Research Center; [3]Department of Neurology and Neurotherapeutics; [4]Department of Neurological Surgery; [5]Harold C. Simmons Cancer Center; and [6]Department of Population and Data Sciences, University of Texas Southwestern Medical Center at Dallas, Dallas, TX

Corresponding Author:
Ananth J. Madhuranthakam, PhD
UT Southwestern Medical Center, 5323 Harry Hines Blvd,
Dallas, TX – 75019-9061;
E-mail: Ananth.Madhuranthakam@UTSouthwestern.edu

Key Words: ASL, perfusion, GBM, reliability, intrasession

Abbreviations:glioblastoma (GBM), pseudocontinuous labeling (pCASL), turbo spin echo (TSE), Cartesian acquisition with spiral profile reordering (CASPR), positron emission tomography (PET), dynamic contrast-enhanced (DSE), dynamic susceptibility contrast (DSC), signal-to-noise ratio (SNR), postlabel delay (PLD), echo time (TE), cerebral blood flow (CBF), normal-appearing gray matter (NAGM), region of interest (ROI)

ABSTRACT

Arterial spin-labeled magnetic resonance imaging can provide quantitative perfusion measurements in the brain and can be potentially used to evaluate therapy response assessment in glioblastoma (GBM). The reliability and reproducibility of this method to measure noncontrast perfusion in GBM, however, are lacking. We evaluated the intrasession reliability of brain and tumor perfusion in both healthy volunteers and patients with GBM at 3 T using pseudocontinuous labeling (pCASL) and 3D turbo spin echo (TSE) using Cartesian acquisition with spiral profile reordering (CASPR). Two healthy volunteers at a single time point and 6 newly diagnosed patients with GBM at multiple time points (before, during, and after chemoradiation) underwent scanning (total, 14 sessions). Compared with 3D GraSE, 3D TSE-CASPR generated cerebral blood flow maps with better tumor-to-normal background tissue contrast and reduced image distortions. The intraclass correlation coefficient between the 2 runs of 3D pCASL with TSE-CASPR was consistently high ($\geq$0.90) across all normal-appearing gray matter (NAGM) regions of interest (ROIs), and was particularly high in tumors (0.98 with 95% confidence interval [CI]: 0.97–0.99). The within-subject coefficients of variation were relatively low in all normal-appearing gray matter regions of interest (3.40%–7.12%), and in tumors (4.91%). Noncontrast perfusion measured using 3D pCASL with TSE-CASPR provided robust cerebral blood flow maps in both healthy volunteers and patients with GBM with high intrasession repeatability at 3 T. This approach can be an appropriate noncontrast and noninvasive quantitative perfusion imaging method for longitudinal assessment of therapy response and management of patients with GBM.

INTRODUCTION

Oncologic patient care and clinical trials are increasingly relying on radiological images for the assessment of therapy response. Currently, the radiological assessment of therapy response is predominantly based on tumor size changes measured using methods such as the Response Evaluation Criteria in Solid Tumors (RECIST) (1) or Response Assessment in Neuro-Oncology (RANO) (2). This is a major limiting factor, as the effects of many therapeutic agents at the microscopic level precede the eventual changes in tumor size. Several quantitative imaging methods are being explored to provide objective measures of microscopic tissue characteristics for early and longitudinal therapy response assessments (3–7). The reliability and reproducibility of these quantitative imaging methods, both in healthy subjects and patients, are warranted for evaluating clinical trials and eventual use in routine clinical practice.

One of the microscopic tumor properties that has gained increased attention is angiogenesis, which is well recognized to support tumor proliferation and infiltration (8). Among various methods to measure angiogenesis (ie, tumor blood supply), arterial spin-labeled (ASL) magnetic resonance imaging (MRI) has emerged as a promising method (9), particularly in the brain (10). Unlike other perfusion-weighted imaging techniques such as positron emission tomography (PET) using ^{15}O-labeled water, ^{99m}Tc-labeled single-photon emission computed tomography, or iodine-based contrast-enhanced computed tomography, MRI

ISSN 2379-1381 https://doi.org/10.18383/j.tom.2020.00010

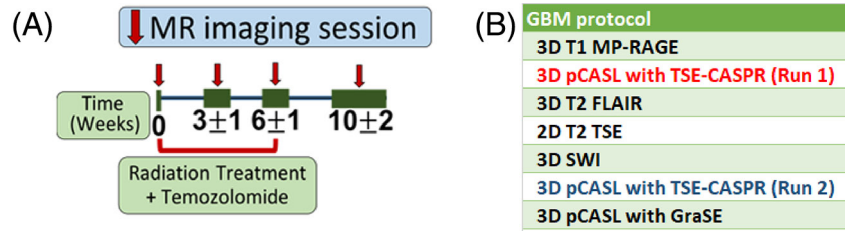

Figure 1. Magnetic resonance imaging (MRI) session time points in patients with GBM (A). MRI including ASL was performed before, during, and after the chemoradiation treatment at the following times (weeks)—week 0: baseline before the treatment; week 3 ± 1: third week of treatment; week 6 ± 1: sixth week of treatment; week 10 ± 2, 4 weeks after the treatment. The MRI protocol includes the 2 repetitions of 3D pseudocontinuous labeling (pCASL) with turbo spin echo Cartesian acquisition with spiral profile reordering (TSE-CASPR) (B).

does not involve ionizing radiation. Furthermore, compared with dynamic contrast-enhanced (DCE) MRI and dynamic susceptibility contrast (DSC) MRI, ASL-MRI uses water as the endogenous tracer and does not require the injection of gadolinium-based contrast agents. Hence, ASL-MRI is well-suited for longitudinal monitoring of patients with cancer without the concerns of nephrogenic systemic fibrosis (11), gadolinium deposition (12), or cumulative radiation exposure (13).

ASL uses the combination of radiofrequency pulses with gradients to magnetically label the blood upstream from the imaging region of interest. After a postlabel delay (PLD), during which the labeled blood perfuses the tissue, its accumulation is measured using standard MR acquisition methods. Because the perfusion replaces only about 1%–2% of the brain water every second, the tissue perfusion is measured by subtracting the labeled image from a control image that does not label the blood upstream. Consequently, ASL images are inherently low in signal-to-noise ratio (SNR) and are commonly acquired using multiple signal averages (14). The low ASL signal is also often compromised by signal variations owing to physiological noise, which is an impediment for accurate and reliable perfusion measurements. Hence, background suppression (BGS) using multiple inversion pulses is highly recommended for ASL acquisitions to minimize these artifacts (15). Therefore, 3D segmented acquisitions like 3D stack-of-spirals using multiple refocusing pulses or 3D gradient and spin echo (GraSE) that use a single excitation per repetition and are optimal for BGS are recommended by the International Society for Magnetic Resonance in Medicine (ISMRM) ASL expert panel consensus for brain imaging (16). Several groups have shown good reliability and reproducibility of ASL-MRI-measured brain perfusion in healthy volunteers using these techniques (17–19). However, all of these acquisition methods are prone to image distortions in areas with increased B0 inhomogeneities such as skull base near bone–air interfaces and in patients with GBM who often undergo craniotomy. Furthermore, automated tumor segmentation algorithms, generated using coregistered anatomical images, are increasingly considered for objective measurements of therapy response (20). Image distortions induced by spiral- or GraSE-based acquisitions make it challenging to accurately coregister and extract various tumor components for longitudinal assessment.

To address these limitations, we recently developed a 3D turbo spin echo (TSE) using Cartesian acquisition with spiral profile reordering (CASPR) combined with pseudocontinuous ASL (pCASL) for robust noncontrast perfusion imaging (21). Brain perfusion images acquired using 3D pCASL with TSE-CASPR showed improved robustness to signal variations and image distortions compared to 3D pCASL with GraSE in healthy volunteers. The purpose of this study was to evaluate the intrasession reliability of brain and tumor perfusion measured using 3D pCASL with TSE-CASPR in both healthy volunteers and patients with GBM at 3 T.

METHODS

Subjects

The study was approved by the institutional review board and written informed consent was obtained from all subjects before participation in the study. Two healthy volunteers (2 females, both 26 years old) and 6 newly diagnosed patients with GBM (female, 1; males, 5; mean age, 58 ± 14 years) were recruited. The 2 healthy volunteers were scanned at a single time point to evaluate the intrasession reliability, while the 6 patients with GBM were enrolled for multiple scans before, during, and after chemoradiation treatment (Figure 1A). In this ongoing study, not all subjects have been scanned at all time points owing to compliance and scheduling issues. However, as we are focused on intrasession reliability in this study, all imaging sessions from different subjects are included for the analysis. Therefore, in total, 14 imaging sessions were performed including healthy volunteers and patients with GBM. The inclusion criteria for the patients were as follows: histologically proven GBM; no prior treatments such as chemotherapy, radiation treatment, and anti-angiogenic therapy, except for surgery; and patients scheduled to undergo standard chemoradiation treatment (6 weeks of external beam radiation therapy with concurrent Temozolomide).

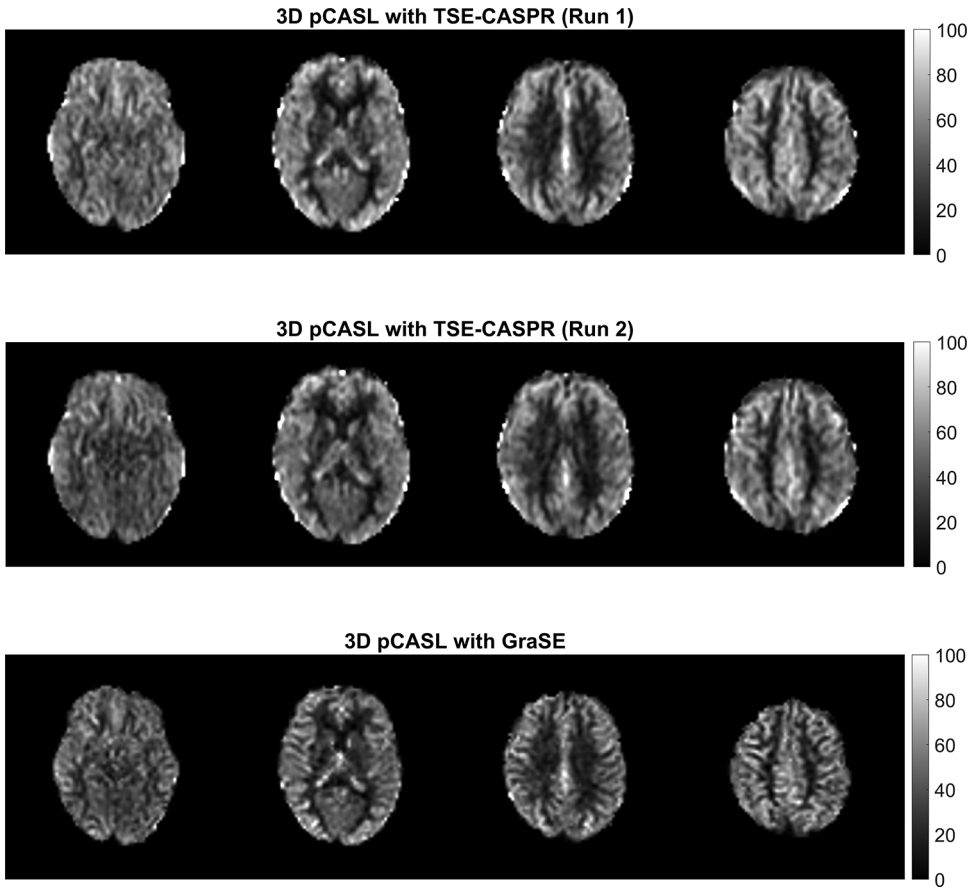

Figure 2. Representative cerebral blood flow (CBF) maps of a 26-year-old healthy female volunteer shown in multiple axial slices acquired during the first run of 3D pCASL with TSE-CASPR (top row), second run of 3D pCASL with TSE-CASPR (middle row), and 3D pCASL with gradient and spin echo (GRASE) (bottom row). Overall, the CBF maps were consistent between different acquisitions. The color bar shows the perfusion values in mL/100 g/min.

MR Imaging

All imaging was performed on a 3 T MR scanner (Ingenia, Philips Healthcare, Best, The Netherlands) using a 32-channel head coil. Brain perfusion was measured using 3D pCASL with TSE-CASPR as described before (21). In brief, labeling was applied with selective radiofrequency pulses (duration = 480 μs, interval = 1210 μs, $B1_{average}$ = 1.07 μT) and corresponding gradients ($G_{average}$ = 0.36 mT/m, G_{max} = 5 mT/m) (22) for 1.8 seconds followed by a 1.8-second PLD before acquisition. The labeling plane was positioned axially across the carotid arteries, right below the cerebellum. BGS was used over the entire imaging volume to reduce the signal from static tissues. BGS used a combination of spatially selective saturation pulses (at 4.7 seconds before acquisition), selective C-shaped frequency offset corrected inversion (C-FOCI) pulse (3.6 seconds before acquisition) (23), and 4 nonselective C-FOCI pulses applied at 1750, 675, 200, and 30 milliseconds before the acquisition to null background tissue signal across a wide range of T1 values. In addition, spatially selective inflow saturation pulses were applied over a 15-cm slab inferior to the labeling plane at 1000, 800, 600, 400 and 200 milliseconds before the acquisition to reduce the post-labeled arterial signal in the major vessels. The ASL data were then acquired using a 3D TSE-CASPR, which used a pseudospiral trajectory on a Cartesian grid with earlier echoes in each echo train sampled at the center of the k-space. This sampling scheme allowed shorter effective echo times (TE_{eff}) and improved the stability of ASL signal by averaging out the signal variations.

In each imaging session, a standard clinical protocol along with 2 repetitions of ASL using 3D TSE-CASPR was performed for each subject (Figure 1B). Gadolinium-based contrast agent (Gadavist) was administered only for the patients with GBM, and hence, DCE-MRI, DSC-MRI, and postcontrast acquisitions were performed only in patients with GBM. 3D pCASL with TSE-CASPR was performed twice in the axial plane, ~20 minutes apart, with the following parameters: TR/TE = 6000/14 milliseconds, FOV = 220 × 220 × 110 mm^3, matrix = 64 × 64, slices = 42, acquired resolution = 3.5 × 3.5 × 6 mm^3, reconstructed resolution = 3 × 3 × 3 mm^3, echo spacing = 2.8 milliseconds, turbo factor = 80, label duration = 1.8 seconds, PLD = 1.8 seconds, signal average = 1, in a 3-minute acquisition. A proton-density-weighted (M_0) image was acquired to calculate quantitative cerebral blood flow (CBF) maps using the same acquisition parameters, but without labeling, BGS, or inflow saturation in 1 minute and 30 seconds. For comparison, ASL images were also acquired using the vendor-supplied 3D pCASL with GraSE acquisition in all subjects matching the same acquisition parameters as 3D pCASL with TSE-CASPR except for: TR/TE = 3900 / 14 milliseconds and signal averages = 3. 3D pCASL with GraSE was acquired in a total scan time of 4 minutes and 30 seconds, including a M_0 acquisition, matching the total acquisition time of 3D pCASL with TSE-CASPR. Therefore, the total acquisition time of 3D pCASL with TSE-CASPR and 3D pCASL with GraSE, both including M0 images, was 4 minutes and 30 seconds each.

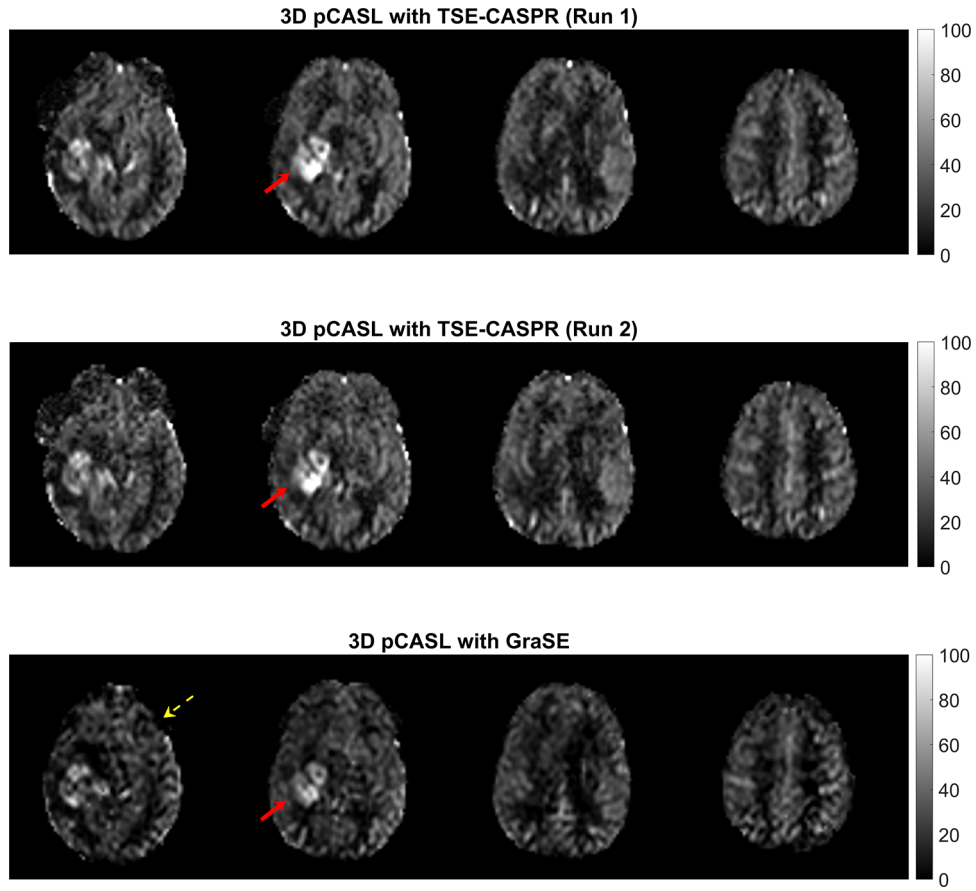

Figure 3. Representative CBF maps of a 47-year-old male patient with GBM shown in multiple axial slices acquired during the first run of 3D pCASL with TSE-CASPR (top row), second run of 3D pCASL with TSE-CASPR (middle row), and 3D pCASL with GraSE (bottom row). Overall, the CBF maps are visually very similar between different acquisitions, including tumor (solid arrow). 3D TSE-CASPR images provided better tumor to background gray matter contrast and are more robust to B0 inhomogeneities when compared with 3D GraSE (dashed arrow). The color bar shows the perfusion values in mL/100 g/min.

Data Processing

3D pCASL with TSE-CASPR images were reconstructed on the scanner using an in-house-developed reconstruction that included complex k-space subtraction (24). The custom-built reconstruction was implemented on the scanner reconstruction platform (Philips recon 2.0), which performed the complex subtraction between the control and label images in the k-space, followed by Fourier transformation to generate the perfusion difference images (ΔM). Voxel-by-voxel perfusion quantification of the brain was performed in MATLAB (The MathWorks, Natick, MA) using Equation (1) with the following parameters: $T1_{blood}$ = 1650 milliseconds, labeling duration (τ) = 1800 milliseconds, PLD = 1800 milliseconds, and tissue-blood partition coefficient (λ) = 0.9 (16). The inversion efficiency of pCASL labeling was 0.8, with an additional inversion efficiency of 0.75 by BGS, which gave the net labeling efficiency (α) = 0.6 (25). CBF maps of 3D pCASL with GraSE images were automatically generated on the scanner using vendor-supplied reconstruction.

$$CBF = \frac{6000 \cdot \lambda \cdot \Delta M \cdot e^{\frac{PLD}{T_{1,blood}}}}{2 \cdot \alpha \cdot T_{1,blood} \cdot M_0 \cdot \left(1 - e^{\frac{-\tau}{T_{1,blood}}}\right)} \text{mL/100g/min} \quad [1]$$

Brain masks of M_0 images were generated with the brain extraction tool in FSL (26–28). For CBF analysis in normal-appearing gray matter (NAGM), all quantitative CBF maps were coregistered and normalized to a standardized space (Montreal Neurological Institute template, MNI space) within FSL by FMRIB's Linear Image Registration Tool (FLIRT) (29, 30). Standard anatomical regions of interest (ROIs) from MNI Structural Atlas including the cerebellum, frontal lobe, parietal lobe, occipital lobe, temporal lobe, putamen, and thalamus were used as templates for the ROI analysis. All ROI templates were applied to the coregistered CBF maps from both 3D pCASL with TSE-CASPR and GraSE. For CBF analysis in tumors, ROIs were manually drawn using free hand tool on visually hyperperfused regions in ASL images using Horos DICOM viewer (Purview, Annapolis, MD). All voxels containing hyperperfused signal on ASL images were included without any specific size limitations. Tumor ROIs were drawn on the first run of 3D pCASL with TSE-CASPR and copied over to the second run. Tumor ROIs were also copied to structural images including 3D T1-weighted MPRAGE (both pre- and postcontrast images), T2-weighted, and T2 FLAIR images for further confirmation.

Statistical Analysis

The mean ± standard deviation (SD) of NAGM and tumor CBF values in mL/100 g/min for both 3D pCASL with TSE-CASPR and 3D pCASL with GraSE were tabulated. The Bland–Altman and linear regression analyses were performed with GraphPad Prism (GraphPad, San Diego, CA). The reliability between the 2 runs of 3D pCASL with TSE-CASPR images were measured using

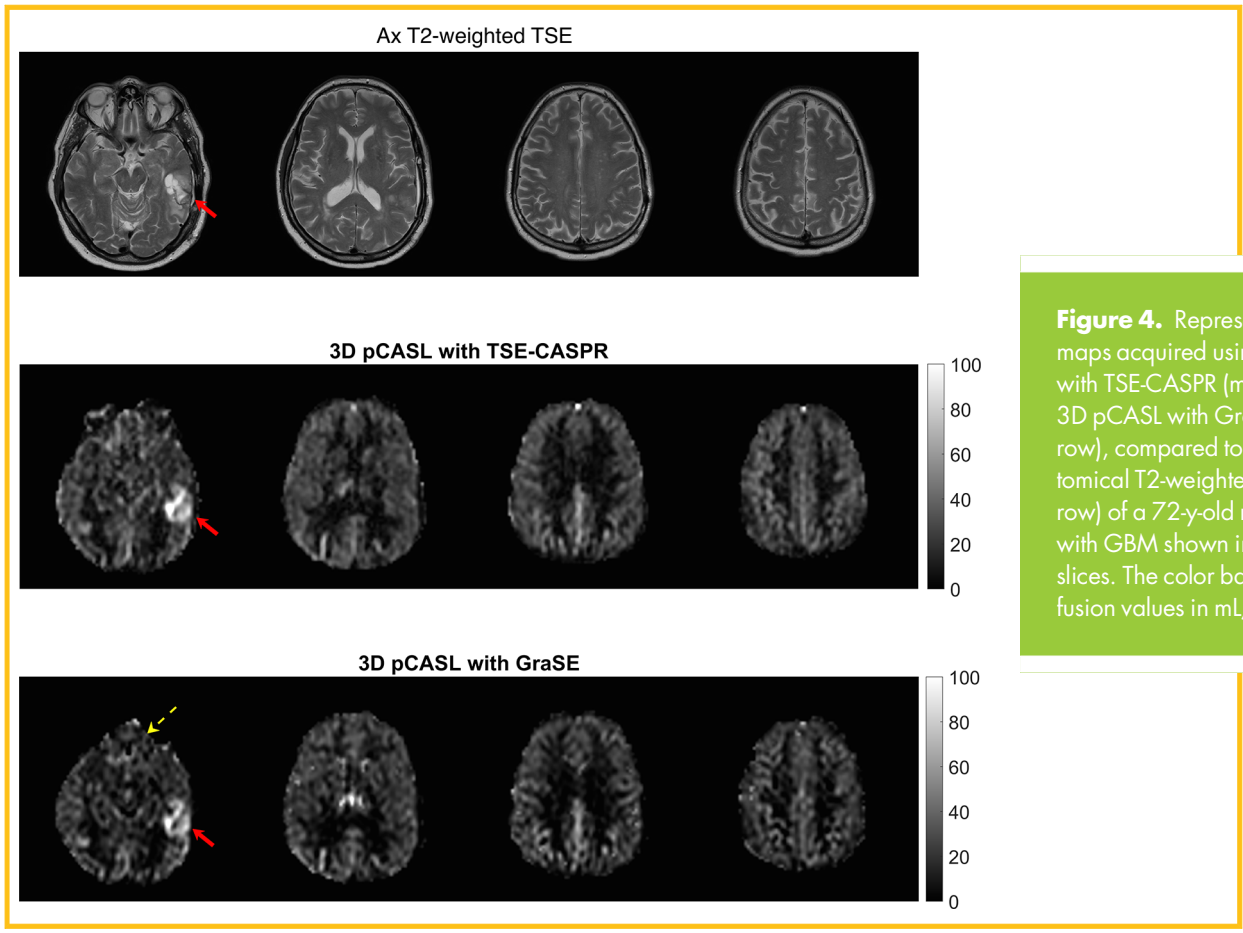

Figure 4. Representative CBF maps acquired using 3D pCASL with TSE-CASPR (middle row) and 3D pCASL with GraSE (bottom row), compared to standard anatomical T2-weighted images (top row) of a 72-y-old male patient with GBM shown in multiple axial slices. The color bar shows the perfusion values in mL/100 g/min.

intraclass correlation coefficient (ICC). ICC estimates and their 95% confidence intervals (CI) were calculated using SPSS statistical package (SPSS, Chicago, IL) based on a single-measurement, absolute-agreement, 2-way mixed-effects model. Within-subject coefficients of variation (wsCV), defined as the ratio of the standard deviation (SD) of the difference between repeated measurements to the mean of the repeated measurements, were also calculated.

RESULTS

Perfusion images of the whole brain were successfully obtained in healthy volunteers and patients with GBM. Representative CBF maps in mL/100 g/min of a 26-year-old healthy volunteer are shown in Figure 2. No major differences were observed in the CBF maps between the 2 runs of 3D pCASL with TSE-CASPR (top 2 rows) and 3D pCASL with GraSE (bottom row). Similar CBF maps were also obtained from all 3 runs of pCASL in patients with GBM (Figure 3). Compared with 3D GraSE, 3D TSE-CASPR generated CBF maps with better tumor-to-normal background tissue contrast (solid arrow) and reduced image distortion (dashed arrow). The increased robustness of 3D TSE-CASPR versus 3D GraSE is more evident in juxtaposition to standard anatomical T2-weighted images (Figure 4). Although the tumor (solid arrow) is clearly visible on all acquisitions, the image distortion seems to displace the tumor posteriorly on 3D GraSE compared to 3D TSE-CASPR and T2-weighted image. Furthermore, there is increased image distortion observed on the 3D GraSE images near sinuses due to higher B0 inhomogeneities (dashed arrows).

The average CBF values along with SD in NAGM and tumors of both 3D pCASL with TSE-CASPR and 3D pCASL with GraSE across 14 imaging sessions for several common ROIs are shown in Table 1 along with the corresponding box and whisker plot in Figure 5. Overall, the CBF values measured using 3D pCASL with TSE-CASPR were slightly higher than the CBF values measured using 3D pCASL with GraSE. Similar lower CBF values using 3D pCASL with GraSE were also observed compared to 2D pCASL with EPI (31). However, the CBF values were consistent between the 2 runs of 3D pCASL with TSE-CASPR showing high correlation in both NAGM (R^2 = 0.91) and tumors (R^2 = 0.96) (Figure 6). Bland–Altman plots together with 95% confidence interval (CI) of the CBF values in NAGM and tumors showed good agreement with minimal bias between the 2 runs of 3D pCASL with TSE-CASPR (Figure 7). The 95% limits of agreement were between ±5 mL/100 g/min for NAGM with 0.16 bias, while it was ±8 mL/100 g/min for tumors with −0.06 bias. The ICC was consistently high (≥0.90) across all NAGM ROIs, and was particularly high in tumors (0.98 with 95% CI: 0.97–0.99) (Table 2). The within-subject coefficients of variation was relatively low in all NAGM ROIs (3.40%–7.12%), and these were also low in tumors (4.91%).

Table 1. Mean ± SD of CBF Values in mL/100g/min Measured Using 3D pCASL with TSE-CASPR and 3D pCASL with GraSE in Multiple ROIs Including Tumor over 14 Imaging Sessions

	Cerebellum	Frontal Lobe	Occipital Lobe	Parietal Lobe	Putamen	Temporal	Thalamus	Tumor
3D TSE-CASPR	30.5 ± 5.2	34.8 ± 9.6	33.9 ± 6.5	35.2 ± 8.3	29.1 ± 7.2	33.0 ± 7.4	30.1 ± 5.5	51.6 ± 19.3
3D GraSE	23.7 ± 4.3	29.6 ± 7.7	29.0 ± 5.7	30.0 ± 6.8	24.3 ± 4.9	27.2 ± 5.6	26.1 ± 4.8	47.5 ± 19.7

DISCUSSION

Tumor angiogenesis is integral to aggressive tumors such as GBM, in that it facilitates tumor growth and infiltration. Noninvasive methods to quantify tumor perfusion at the baseline (before therapy initiation) and more importantly for longitudinal assessment of therapy response will be beneficial for personalized patient care. ASL-MRI has recently emerged as a noninvasive quantitative perfusion imaging technique and is commercially available for brain imaging on MR scanners from major vendors. Although several groups have previously reported the good reliability and reproducibility of ASL-measured noncontrast perfusion in the brain, almost all studies have been performed in normal healthy volunteers. Chen et al. showed high intrasession reliability (low wsCV < 5%) and good intersession reproducibility (wsCV < 10%) in 12 healthy volunteers (17). Similarly, Wu et al. showed consistently high intra- and interscanner reproducibility, with ICC >0.95 and 0.92, respectively, in 8 healthy volunteers (19). Based on these works, ASL consistently showed good reliability in healthy volunteers. Additionally, Xu et al. have performed intrasession reliability of ASL-MRI in elderly patients with mild cognitive impairment (MCI) and Alzheimer disease (AD) with good ICC (>0.9) (32). Kilroy et al. have performed a test–retest reproducibility in MCI and AD subjects with moderate ICC (0.7) (33). However, none of the repeatability studies have been performed in patients with brain tumor. To the best of our knowledge, this study is the first report of intrasession reliability of ASL-measured noncontrast perfusion in brain tumors.

There have been several different flavors of ASL preparation methods and data acquisition methods that have been developed by various groups. The introduction of pseudocontinuous ASL (pCASL) (34) and the endorsement of this technique by the perfusion study group of ISMRM (16), propelled pCASL as the foremost technique to measure brain perfusion owing to its increased SNR and compatibility on modern clinical scanners. This consensus paper also recommended stack-of-spirals or 3D GraSE techniques as preferred readouts owing to their compatibility with BGS to minimize physiological and instrumentational noise. However, these data acquisition methods are more sensitive to B0 inhomogeneities (35), which are increasingly encountered in patients with GBM, who often undergo craniotomy and also often contain intratumoral hemorrhage. The 3D TSE acquisition using Cartesian sampling (ie, TSE-CASPR) that we have previously developed (21) addresses these shortcomings and shows increased robustness to image artifacts. In this study, we showed the high intrasession reliability of this method in measuring

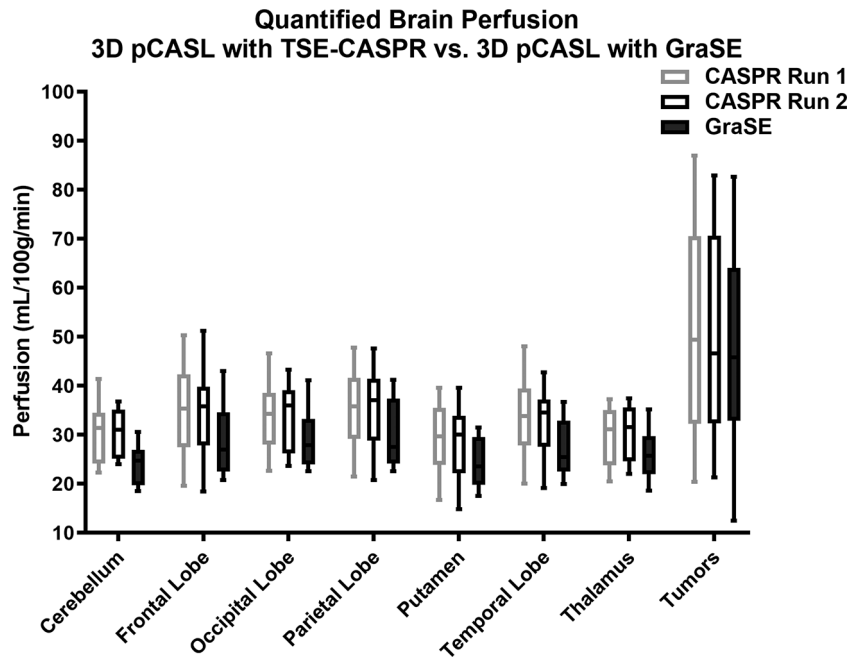

Figure 5. Quantified CBF measurements in all regions of interest (ROIs) from normal-appearing gray matter (NAGM) and tumor regions across all the imaging sessions for both runs of 3D pCASL with TSE-CASPR and 3D pCASL with GraSE. The CBF values are consistent between the 2 runs of 3D pCASL with TSE-CASPR and very similar when compared with 3D pCASL with GraSE.

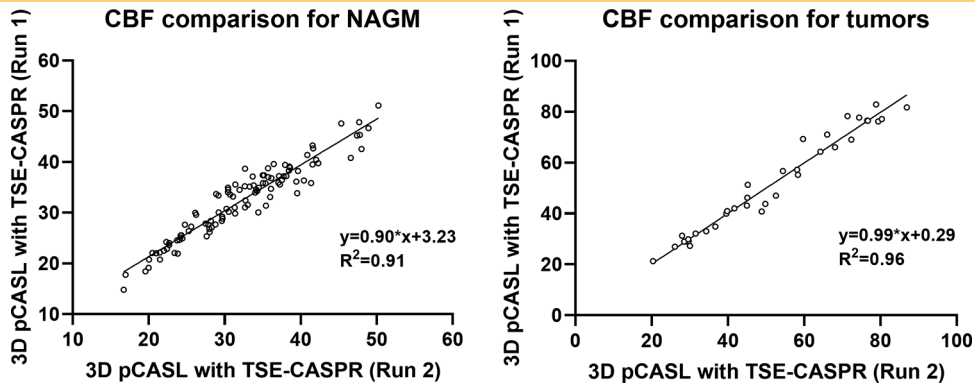

Figure 6. Correlation plots of 2 CBF measurements in mL/100g/min using 3D pCASL with TSE-CASPR from all ROIs in 14 imaging sessions, measured in NAGM (left) and in the tumors (right). The estimated linear regressions show excellent linear correlation between the 2 runs of 3D pCASL with TSE-CASPR-measured CBF values.

brain perfusion in both healthy volunteers and in patients with GBM, including tumor perfusion (≥0.9 ICC).

Compared to other perfusion methods, there are several advantages to ASL-measured noncontrast perfusion. ASL does not use exogenous contrast agent and are very amenable for repeated studies. While gadolinium-based contrast agent administered DCE or DSC-MRI can be performed to measure blood flow, these techniques are semiquantitative and are sensitive to mathematical modeling and fitting algorithms (36, 37). Even using a digitally generated data set with DSC-MRI acquisition parameters (38), Bell et al. have reported significant variations in the pharmacokinetic parameters based on the underlying analysis software (39). The quantitative analysis of ASL-measured perfusion is relatively simple and requires only the M_0 image using the same acquisition parameters as the ASL image (Equation [1]). This simplifies the quantitative analysis, making the ASL measurement relatively insensitive to modeling errors, which is an important feature to enable robust and reliable quantitative measurements. Furthermore, the use of exogenous contrast agents limits the capability of performing repeatability studies using DCE- or DSC-MRI.

We have also developed a 3D-printed perfusion phantom for the assessment of ASL-measured noncontrast perfusion (40). This phantom enables the development of quality control protocols that can be used to assess the performance of ASL-MRI technique. The use of 3D stack-of-spirals or 3D GraSE techniques is often challenging in such small phantoms owing to low coil loading and increased B0 inhomogeneities. The 3D TSE-CASPR acquisition, with its increased robustness to B0 inhomogeneities, can enable this analysis in the perfusion phantom. As part of the Quantitative Imaging Network (QIN) collaborative projects, future work will consider a multisite evaluation of 3D pCASL with TSE-CASPR using this 3D-printed perfusion phantom. This will facilitate the quality assurance and quality control protocols for the eventual use of ASL-MRI-measured noncontrast perfusion in clinical trials and in routine patient care.

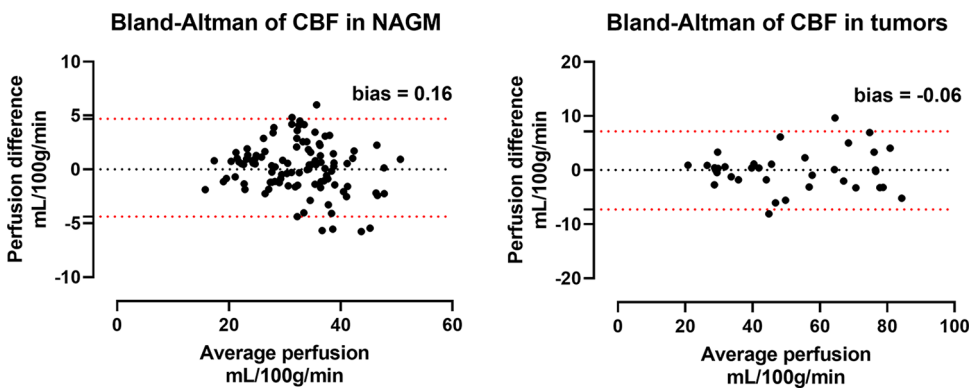

Figure 7. Bland–Altman analysis measured across all ROIs in 14 imaging sessions showed no significant bias between the 2 runs of 3D pCASL with TSE-CASPR. 95% confidence intervals of the agreement are shown in red dashed line. The left plot shows CBF values from NAGM, and the right plot shows CBF values from tumors, suggesting good agreement with minimal bias.

Table 2. Intraclass Correlation Coefficient (ICC) and Within-Subject Coefficient of Variation (wsCV) Observed for CBF Measurements Between the 2 Runs of 3D pCASL with TSE-CASPR

	Cerebellum	Frontal Lobe	Occipital Lobe	Parietal Lobe	Putamen	Temporal	Thalamus	NAGM[a]	Tumor
ICC	0.91	0.98	0.92	0.98	0.90	0.95	0.95	0.95	0.98
95% CI	0.76–0.97	0.95–0.99	0.79–0.97	0.94–0.99	0.74–0.97	0.95–0.98	0.86–0.98	0.93–0.97	0.97–0.99
wsCV (%)	4.42	3.95	5.13	3.40	7.12	4.94	4.08	4.81	4.91

[a] Normal-appearing gray matter (NAGM) includes all gray matter ROIs.

There are several limitations to our study. First, we performed only intrasession reliability of 3D pCASL with TSE-CASPR in this preliminary evaluation. For eventual use of any quantitative imaging technique, both intrasession reliability and intersession reproducibility are required. Future studies will perform these assessments in both patients with GBM and age-matched healthy volunteers. Second, we evaluated this technique in only 6 patients with GBM, but imaged at multiple sessions. However, these data are from an ongoing clinical study (Clinical trial: NCT03922984), and we anticipate to have more subjects at the conclusion of the study. Third, we performed the reliability of 3D pCASL with TSE-CASPR, but not with 3D pCASL with GraSE owing to limited scan time. However, 3D pCASL with GraSE was acquired using 3 signal averages in our study to improve the SNR. We will consider each of these signal averages as a separate acquisition and evaluate the intrasession repeatability in patients with GBM on a larger cohort. Furthermore, we will consider multiple acquisitions using 3D pCASL with GraSE in healthy volunteers. Finally, we used automated methods to extract ROIs in multiple gray matter regions by registering the ASL images to MNI space but manual segmentation was used to extract the tumor ROIs. Although precautions were taken to extract the same tumor ROIs between multiple acquisitions, these ROIs are subjective. We are developing automated tumor segmentation algorithms using convolutional neural networks (41) for objective assessment of tumor ROIs that can be used for future analysis. The improved robustness of 3D TSE-CASPR with minimal to nonexistent image distortion will readily facilitate this automated tumor segmentation even in ASL images.

In conclusion, 3D pCASL with TSE-CASPR provided robust CBF maps in both healthy volunteers and patients with GBM with high intrasession repeatability at 3 T. This approach can be an appropriate noncontrast and noninvasive quantitative imaging method for longitudinal assessment of therapy response and management of patients with GBM.

ACKNOWLEDGMENTS

Equal contribution: L.Z. and Y.W. contributed equally to this work.
This work was supported by NIH/NCI grant U01CA207091. We thank Kelli Key, PhD, and Abey Thomas, RT (MR), for their help in human imaging, and Ben Wagner, MSEE, for his help with image database and analysis routines.

Disclosures: The authors have nothing to disclose.

Conflict of Interest: None reported.

REFERENCES

1. Eisenhauer EA, Therasse P, Bogaerts J, Schwartz LH, Sargent D, Ford R, Dancey J, Arbuck S, Gwyther S, Mooney M, Rubinstein L, Shankar L, Dodd L, Kaplan R, Lacombe D, Verweij J. New response evaluation criteria in solid tumours: revised RECIST guideline (version 1.1). Eur J Cancer. 2009;45:228–247.
2. Wen PY, Chang SM, Van den Bent MJ, Vogelbaum MA, Macdonald DR, Lee EQ. Response assessment in neuro-oncology clinical trials. J Clin Oncol. 2017;35:2439–2449.
3. Gatenby RA, Grove O, Gillies RJ. Quantitative imaging in cancer evolution and ecology. Radiology. 2013;269:8–15.
4. Yankeelov TE, Mankoff DA, Schwartz LH, Lieberman FS, Buatti JM, Mountz JM, Erickson BJ, Fennessy FMM, Huang W, Kalpathy-Cramer J, Wahl RL, Linden HM, Kinahan PE, Zhao B, Hylton NM, Gillies RJ, Clarke L, Nordstrom R, Rubin DL. Quantitative imaging in cancer clinical trials. Clin Cancer Res. 2016;22:284–290.
5. Nordstrom RJ. The Quantitative Imaging Network in precision medicine. Tomography. 2016;2:239–241.
6. Farahani K, Kalpathy-Cramer J, Chenevert TL, Rubin DL, Sunderland JJ, Nordstrom RJ, Buatti J, Hylton N. Computational challenges and collaborative projects in the NCI Quantitative Imaging Network. Tomography. 2016;2:242–249.
7. Yankeelov TE. The Quantitative Imaging Network: a decade of achievement. Tomography. 2019;5:A8.
8. Folkman J. The role of angiogenesis in tumor growth. Semin Cancer Biol. 1992;3:65–71.
9. Zhang Y, Kapur P, Yuan Q, Xi Y, Carvo I, Signoretti S, Dimitrov I, Cadeddu JA, Margulis V, Muradyan N, Brugarolas J, Madhuranthakam AJ, Pedrosa I. Tumor vascularity in renal masses: correlation of arterial spin-labeled and dynamic contrast-enhanced magnetic resonance imaging assessments. Clin Genitourin Cancer. 2016;14:e25–36.
10. Noguchi T, Yoshiura T, Hiwatashi A, Togao O, Yamashita K, Nagao E, Shono T, Mizoguchi M, Nagata S, Sasaki T, Suzuki SO, Iwaki T, Kobayashi K, Mihara F, Honda H. Perfusion imaging of brain tumors using arterial spin-labeling: correlation with histopathologic vascular density. AJNR Am J Neuroradiol. 2008;29:688–693.
11. Saleh L, Juneman E, Movahed MR. The use of gadolinium in patients with contrast allergy or renal failure requiring coronary angiography, coronary intervention, or vascular procedure. Catheter Cardiovasc Interv. 2011;78:747–754.
12. McDonald RJ, McDonald JS, Kallmes DF, Jentoft ME, Murray DL, Thielen KR, Williamson EE, Eckel LJ. Intracranial gadolinium deposition after contrast-enhanced MR imaging. Radiology. 2015;275:772–782.
13. Mulvihill DJ, Jhawar S, Kostis JB, Goyal S. Diagnostic medical imaging in pediatric patients and subsequent cancer risk. Acad Radiol. 2017;24:1456–1462.
14. Alsop DC, Detre JA. Multisection cerebral blood flow MR imaging with continuous arterial spin labeling. Radiology. 1998;208:410–416.
15. Ye FQ, Frank JA, Weinberger DR, McLaughlin AC. Noise reduction in 3D perfusion imaging by attenuating the static signal in arterial spin tagging (ASSIST). Magn Reson Med. 2000;44:92–100.
16. Alsop DC, Detre JA, Golay X, Günther M, Hendrikse J, Hernandez-Garcia L, Lu H, MacIntosh BJ, Parkes LM, Smits M, van Osch MJP, Wang DJJ, Wong EC, Zaharchuk G. Recommended implementation of arterial spin-labeled perfusion MRI for clinical applications: a consensus of the ISMRM Perfusion Study Group and the European Consortium for ASL in Dementia. Magn Reson Med. 2015;73:102–116.
17. Chen Y, Wang DJ, Detre JA. Test-retest reliability of arterial spin labeling with common labeling strategies. J Magn Reson Imaging. 2011;33:940–949.

18. Mutsaerts HJMM, Steketee RME, Heijtel DFR, Kuijer JPA, van Osch MJP, Majoie CBLM, Smits M, Nederveen AJ. Inter-vendor reproducibility of pseudo-continuous arterial spin labeling at 3 Tesla. PLoS One. 2014;9:e104108.
19. Wu B, Lou X, Wu X, Ma L. Intra- and interscanner reliability and reproducibility of 3D whole-brain pseudo-continuous arterial spin-labeling MR perfusion at 3T. J Magn Reson Imaging. 2014;39:402–409.
20. Meier R, Knecht U, Loosli T, Bauer S, Slotboom J, Wiest R, Reyes M. Clinical evaluation of a fully-automatic segmentation method for longitudinal brain tumor volumetry. Sci Rep. 2016;6:23376.
21. Greer JS, Wang X, Wang Y, Pinho MC, Maldjian JA, Pedrosa I, Madhuranthakam AJ. Robust pCASL perfusion imaging using a 3D Cartesian acquisition with spiral profile reordering (CASPR). Magn Reson Med. 2019;82:1713–1724.
22. Zhao L, Vidorreta M, Soman S, Detre JA, Alsop DC. Improving the robustness of pseudo-continuous arterial spin labeling to off-resonance and pulsatile flow velocity. Magn Reson Med. 2017;78:1342–1351.
23. Wang X, Greer JS, Dimitrov IE, Pezeshk P, Chhabra A, Madhuranthakam AJ. Frequency offset corrected inversion pulse for B0 and B1 insensitive fat suppression at 3T: application to MR neurography of brachial plexus. J Magn Reson Imaging. 2018;48:1104–1111.
24. Wang Y, Greer JS, Wigal T Pinho MC, Maldjian JA, Madhuranthakam AJ. Compensating T2 blurring in 3D TSE with Cartesian acquisition based arterial spin labeled MRI. In: Proceedings of the 27th Annual Meeting of ISMRM, Montreal, QC, Canada. 2019:4962.
25. Garcia DM, Duhamel G, Alsop DC. Efficiency of inversion pulses for background suppressed arterial spin labeling. Magn Reson Med. 2005;54:366–372.
26. Woolrich MW, Jbabdi S, Patenaude B, Chappell M, Makni S, Behrens T, Beckmann C, Jenkinson M, Smith SM. Bayesian analysis of neuroimaging data in FSL. Neuroimage. 2009;45:S173–86.
27. Smith SM, Jenkinson M, Woolrich MW, Beckmann CF, Behrens TEJ, Johansen-Berg H, Bannister PR, De Luca M, Drobnjak I, Flitney DE, Niazy RK, Saunders J, Vickers J, Zhang Y, De Stefano N, Brady JM, Matthews PM. Advances in functional and structural MR image analysis and implementation as FSL. Neuroimage. 2004;23:S208–19.
28. Jenkinson M, Beckmann CF, Behrens TE, Woolrich MW, Smith SM. FSL. Neuroimage. 2012;62:782–790.
29. Jenkinson M, Smith S. A global optimisation method for robust affine registration of brain images. Med Image Anal. 2001;5:143–156.
30. Jenkinson M, Bannister P, Brady M, Smith S. Improved optimization for the robust and accurate linear registration and motion correction of brain images. Neuroimage. 2002;17:825–841.
31. Baas KPA, Mutsaerts HJMM, Petr J, Kuijer JPA, van de Ven KCC, (Eds). Comparing pCASL CBF measurements between 3D-GraSE and 2D-EPI on 1.5T and 3T systems. In: Proceedings of the 26th Annual Meeting of ISMRM; 2018; Paris.
32. Xu G, Rowley HA, Wu G, Alsop DC, Shankaranarayanan A, Dowling M, Christian BT, Oakes TR, Johnson SC. Reliability and precision of pseudo-continuous arterial spin labeling perfusion MRI on 3.0 T and comparison with 15O-water PET in elderly subjects at risk for Alzheimer's disease. NMR Biomed. 2010;23:286–293.
33. Kilroy E, Apostolova L, Liu C, Yan L, Ringman J, Wang DJ. Reliability of two-dimensional and three-dimensional pseudo-continuous arterial spin labeling perfusion MRI in elderly populations: comparison with 15O-water positron emission tomography. J Magn Reson Imaging. 2014;39:931–939.
34. Dai W, Garcia D, de Bazelaire C, Alsop DC. Continuous flow-driven inversion for arterial spin labeling using pulsed radio frequency and gradient fields. Magn Reson Med. 2008;60:1488–1497.
35. Li Z, Schär M, Wang D, Zwart NR, Madhuranthakam AJ, Karis JP, Pipe JG. Arterial spin labeled perfusion imaging using three-dimensional turbo spin echo with a distributed spiral-in/out trajectory. Magn Reson Med. 2016;75:266–273.
36. Huang W, Chen Y, Fedorov A, Li X, Jajamovich GH, Malyarenko DI, Aryal MP, LaViolette PS, Oborski MJ, O'Sullivan F, Abramson RG, Jafari-Khouzani K, Afzal A, Tudorica A, Moloney B, Gupta SN, Besa C, Kalpathy-Cramer J, Mountz JM, Laymon CM, Muzi M, Schmainda K, Cao Y, Chenevert TL, Taouli B, Yankeelov TE, Fennessy F, Li X. The impact of arterial input function determination variations on prostate dynamic contrast-enhanced magnetic resonance imaging pharmacokinetic modeling: a multicenter data analysis challenge. Tomography. 2016;2:56–66.
37. Huang W, Chen Y, Fedorov A, Li X, Jajamovich GH, Malyarenko DI, Aryal MP, LaViolette PS, Oborski MJ, O'Sullivan F, Abramson RG, Jafari-Khouzani K, Afzal A, Tudorica A, Moloney B, Gupta SN, Besa C, Kalpathy-Cramer J, Mountz JM, Laymon CM, Muzi M, Kinahan PE, Schmainda K, Cao Y, Chenevert TL, Taouli B, Yankeelov TE, Fennessy F, Li X. The impact of arterial input function determination variations on prostate dynamic contrast-enhanced magnetic resonance imaging pharmacokinetic modeling: a multicenter data analysis challenge. Tomography. 2019;5:99–109.
38. Semmineh NB, Stokes AM, Bell LC, Boxerman JL, Quarles CC. A population-based digital reference object (DRO) for optimizing dynamic susceptibility contrast (DSC)-MRI methods for clinical trials. Tomography. 2017;3:41–49.
39. Bell LC, Semmineh N, An H, Eldeniz C, Wahl R, Schmainda KM, Prah MA, Erickson BJ, Korfiatis P, Wu C, Sorace AG, Yankeelov TE, Rutledge N, Chenevert TL, Malyarenko D, Liu Y, Brenner A, Hu LS, Zhou Y, Boxerman JL, Yen Y-F, Kalpathy-Cramer J, Beers AL, Muzi M, Madhuranthakam AJ, Pinho M, Johnson B, Quarles CC. Evaluating multisite rCBV consistency from DSC-MRI imaging protocols and postprocessing software across the NCI Quantitative Imaging Network sites using a digital reference object (DRO). Tomography. 2019;5:110–117.
40. Greer JS, Wang X, Wang Y, Hulsey K, Lenkinski RE, Madhuranthakam AJ. A 3D printed perfusion phantom for quality controlled measurement of arterial spin labeled perfusion. In: Proceedings of the 25th Annual Meeting of ISMRM, Honolulu, HI, USA. 2017:3805.
41. Yogananda CGB, Shah BR, Vejdani-Jahromi M, Nalawade SS, Murugesan GK, Yu FF, Pinho MC, Wagner BC, Mickey B, Patel TR, Fei B, Madhuranthakam AJ, Maldjian JA. A novel fully automated MRI-based deep learning method for classification of Idh Mutation Status in Brain Gliomas. Neuro Oncol. 2020;22:402–411.